Stochastic modeling of multi-filament yarns. I. Random properties within the cross-section and size effect

R. Chudoba [a,*], M. Vořechovský [b], M. Konrad [a]

[a] *Structural Statics and Dynamics, Aachen University of Technology, Mies-van-der-Rohe-Str. 1, 52056 Aachen, Germany*
[b] *Institute of Structural Mechanics, Technical University Brno, Veveří 95, 602 00 Brno, Czech Republic*

Abstract

The paper presents a thorough study of sources of randomness/disorder in multi-filament yarns that are relevant for their performance in textile reinforced concrete. For the analysis of bundles with infinite number of fibers we use a continuous analytical model with refined kinematic hypothesis. In parallel, we apply a more general discrete numerical bundle model covering the cases of finite number of fibers and spatial variations of material properties. The considered distributions of material properties include variations of parameters (local stiffness and strength) both from filament to filament and over the length of each filament. In the present paper, we study the influence of variations in filament properties across the bundle. In the companion paper (Vořechovský, M., Chudoba, R., 2006. Stochastic modeling of multi-filament yarns. II. Random properties over the length and size effect. International Journal of Solids and Structures), the variations of material properties over the length are considered. Both papers provide the basis for correct interpretation of the data obtained from the tensile test on multi-filament yarn with varied specimen length. As the actual goal of the present work is to derive yarn characteristics relevant for crack bridges in cementitious composites we systematically assess the significance of the studied sources of disorder in the context of extremely short bundle lengths.
© 2005 Elsevier Ltd. All rights reserved.

Keywords: Multi-filament yarn; Fiber bundle models; Delayed activation; Size effect

---
* Corresponding author. Tel.: +422418050289; fax: +422418022303.
 E-mail addresses: rch@lbb.rwth-aachen.de, rch@baustatik-aachen.de (R. Chudoba), vorechovsky.m@fce.vutbr.cz (M. Vořechovský), konrad@lbb.rwth-aachen.de (M. Konrad).

R. Chudoba et al. / International Journal of Solids and Structures 43 (2006) 413–434

Nomenclature

A	cross-sectional area
COV	coefficient of variation
D	filament diameter
e	bundle strain
E	Young's modulus
$G_i(\theta_i)$	cumulative probability distribution of a random parameter
$H(\cdot)$	Heaviside unit step function
$M_\theta(e)$, $M_0(e)$	mean load–strain function of an imperfect and perfect bundle
$q_{e,i}(e)$, $q_{\varepsilon,i}(\varepsilon_i)$	global and local representation of the constitutive law
T	wave period
$T^{(+)}$, $T^{(-)}$	yarn force before and after filament rupture
$T(e)$	load–strain function of the bundle
l	nominal length of the test specimen
n	number of filaments in the bundle
p	number of material point, finite elements
$w(\chi, \alpha)$	function describing the filament position in the bundle
$\mathscr{R}$	set of points representing the bundle load–strain diagram
α	general parameter for the mapping: filament $\rightarrow$ bundle
ε	filament strain (intrinsic)
λ	ratio of extra (stretched) filament length to the nominal length
σ	tensile strength
θ	filament activation strain (slack)
ξ	filament breaking strain
$\mu_\theta(e)$, $\mu_0(e)$	mean load–strain function of the filament with and without imperfections
$\boldsymbol{\theta}$	random vector parameter

1. Introduction

Composite materials combining cementitious matrix with textile reinforcement have become a subject of intensive research in the last decade (Curbach and Hegger, 2001). Forming flexibility of textile structures and quasi-ductile behavior of the produced composites opens up new possibilities especially in two application areas of civil engineering:

- production of efficient light-weight structural elements (Hegger, 2002) and
- strengthening and retrofitting of existing buildings (Curbach, 2002).

The heterogeneous nature of the reinforcement and of the matrix introduces sources of randomness at several scales of the material structure. For robust modeling of the overall material behavior it is inevitable to identify and analyze the sources of randomness both experimentally and theoretically. The need for a sound description of the length-dependent behavior of reinforcing yarns is documented in Fig. 1. The performance measured in the tensile test with $l_{\text{test}} \approx 0.1$ m must be extrapolated to application-relevant effective lengths, namely to the effective length occurring in a crack bridge ($l_{\text{bridge}} \approx 0.0001$ m) and/or to the length of a structure ($l_{\text{struct}} \geqslant 1$ m).
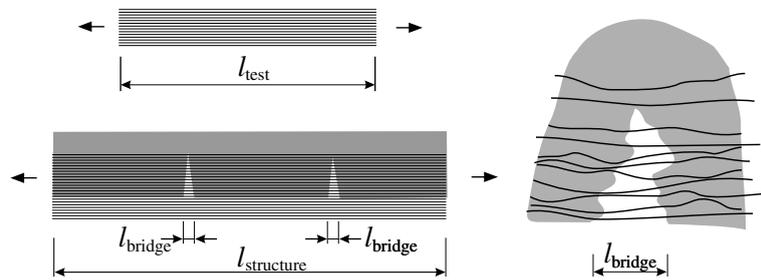
Fig. 1. Effective lengths.

For such an extrapolation, the length-dependent performance must be captured in terms of the fundamental failure and interaction mechanisms as they develop during the loading. Obviously, the way of propagation of these mechanisms to the global failure is strongly influenced by the statistical properties of the yarn structure. In the particular case of very short effective length l_{bridge}, even small irregularities in the material structure (i.e. differences in filament lengths or activation strains) have dominant influence on the overall performance and cannot be disregarded. However, the conditions of a crack bridge cannot be reproduced in the laboratory tests.

On the other hand, for large effective lengths the overall bundle strength is governed by the scatter of strength along the bundle (statistical size effect). The natural way to obtain the statistical strength distribution would be to perform filament tensile tests. However, for the tested high-modulus brittle material this test turned out to be expensive and very difficult to construct in a reproducible manner.

In order to circumvent these difficulties we performed tensile tests on bundles with varied length. By applying a versatile numerical model we could obtain both the filament data and data characterizing the structure of the bundle by inverse identification. In other words, the length-dependent response of a yarn in the tensile test served as an additional source of information to be exploited in the model with the ambition to extrapolate the data to the conditions occurring in real applications. For this purpose we performed parametric studies of length-dependent yarn performance for various sources of randomness/disorder. In spite of the specific motivation, the results can be seen as a general contribution to the description of the complex size effect inherent to multi-filament bundles.

In order to capture the effect of disorder in the yarn structure on the overall performance the statistical approach is inevitable. The basis for statistical modeling of multi-filament bundles has been established by Fisher and Tippett (1928) and Weibull (1939) in form of the weakest-link model. This concept has been applied in the formulation of the fiber bundle models (FBM) originally introduced by Daniels (1945) and Coleman (1958). The FBMs are constructed as a parallel set of fibers, each of which has Weibull distribution of strength (Phoenix, 1978; Harlow and Phoenix, 1978a,b; Smith and Phoenix, 1981). Fibers break if the acting load exceeds their local strength. Upon the fiber failure, there are two possible rules for the stress redistribution: (1) global load sharing (GLS) with equal redistribution of the load among all intact and active fibers (filaments) remaining in the set, and (2) some type of local load sharing (LLS) where the force released by the broken fiber is transferred to its nearest neighbors.

The strength-based formulation of the FBMs have been modified by Phoenix and Taylor (1973) into more flexible strain-based form providing an explicit expressions for a mean load–deformation curve and the associated covariance. Using this formulation, the asymptotic distribution for general nonlinear stress–strain diagram of a single fiber and for the number of fibers growing infinitely large has been presented in Phoenix (1974). The superior feature of this formulation is the possibility to combine variations in strength with the variation in other material parameters, like filament length, activation strain and local

stiffness. Using this model, an investigation of the random slack (delayed activation) of filaments has been presented in Phoenix (1975). Using a modified kinematic hypothesis Phoenix (1979) extended the strain-based bundle model for twisted yarn structures.

The FBMs provided a basis for successful micromechanical models considering localization (Beyerlein and Phoenix, 1997), the effect of the matrix between the filaments (Phoenix et al., 1997) and the nonlinear behavior (Krajcinovic and Silva, 1982). Extensions of FBMs have been introduced taking into account the possible multiple cracking of filaments by replacing the brittle filament failure with a continuous damage parameter (Kun et al., 2000). In order to study more complex interaction patterns, the FBMs must be replaced by a deterministic micromechanical model combined with full Monte-Carlo simulation technique. This approach has been used to analyze the influence of different fiber arrangements on the stress concentration around the broken fibers (Ibnabdeljalil and Curtin, 1997). The prohibitive computational costs have been reduced by simplified micromechanical models like break-influence superposition based on the shear-lag model (Beyerlein and Phoenix, 1996) or the lattice Green's function technique adopted to composite failure (Zhou and Curtin, 1995). Another source of randomness in form of interaction patterns randomly distributed over the yarn has been studied by Hidalgo et al. (2002). The disordered structure of filaments has been captured by continuous redistribution law ranging from the LLS to GLS rules and randomizing the interaction diameter in a Monte-Carlo simulation.

In the present study, we shall follow two modeling concepts. First, we use a simple deterministic model of bundle with discrete resolution of individual filaments and combine it with a stochastic simulation. Second, we compare the numerical results with the analytical asymptotic solution for mean bundle response introduced by Phoenix and Taylor (1973). In the simulation we include sources of randomness stemming both from the yarn structure and from the experimental setup.

In particular, it is inevitable to include the influence of delayed activation and varying filament length. Furthermore, for some types of yarns (e.g. AR-glass) there are also differences between cross-sectional area of individual filaments. By considering these cross-sectional variations of filament properties together with the spatial variations of material properties along the yarn in a single model we are able to capture/reproduce the whole loading and failure process during the test, size effect inclusive (Vořechovský and Chudoba, 2006). As a result, we obtain more information about the filament properties and their interactions in the bundle. The filament bundle model capturing all the interacting effects occurring in the tensile experiment with varied specimen length provides the stepping stone for robust modeling of the failure process in the crack bridges of the textile-reinforced concrete.

In the present paper we first describe the effects occurring during the tensile experiment of the yarn with the special focus on yarn types used in the textile reinforced concrete (TRC), see Section 2. After that, we introduce the numerical and analytical models covering the effects identified in the tensile experiment (Section 3) and study their qualitative influence on the load–strain diagram (Section 4). The influence of delayed activation is then studied on selected wave patterns in detail (Section 5) and discussed in connection with the performed experiments in Section 6. In the companion paper (Vořechovský and Chudoba, 2006) we study the influence of random spatial distribution of local strength and local material stiffness along filaments. In the same paper, the resulting size effect (bundle strength dependence on the length) is studied with and without the effect of delayed activation.

2. Effects included in the tensile test

As already quoted in the introduction there are two major reasons for constructing the model: (1) detailed interpretation of the experimental data obtained from the tensile test with different yarn lengths and (2) prediction of the yarn behavior in crack bridges of brittle cementitious composites. In this section, we shall review the observable effects that should be reproduced by the model.
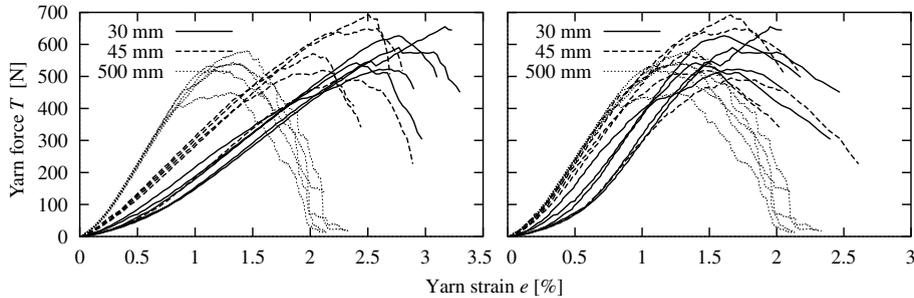
Fig. 2. Tensile tests on AR-glass yarns with varied length. Left: raw data. Right: corrected data by subtracting the deformation of the epoxy clamping.

Fig. 2(left) shows the load–strain curves obtained from the tensile test on AR-glass yarns with lengths varied in the range from 30 to 500 mm. The loading rate has been set to 1% strain in a minute. The response curves allow us to identify the following effects:

A. Gradual growth of stiffness in the initial stages of loading. This phenomenon gets amplified for short specimens.
B. Reduction of bundle strength and maximum bundle strain with increasing specimen length.
C. Reduction of bundle stiffness with decreasing length of the specimen.
D. Reduction of scatter of stiffness and of bundle strength with increasing specimen length.
E. Brittle failure of short specimens as opposed to ductile failure of long specimens.

In order to model the yarn behavior in various loading conditions these complex effects must be explained and quantified in terms of simpler or even elementary effects that may be appointed (1) to the material constituents, i.e. the individual filaments, (2) to the filament ensemble or (3) to the experimental setup.

In the first case, linear elastic brittle behavior (AR-glass) is assumed. Its characteristics (strength $\sigma(\chi)$, material stiffness $E(\chi)$ and area $A(\chi)$) may exhibit variations along the filament: as shown in Fig. 3a. If there are flaws in the glass microstructure, there may also be locally concentrated reductions of strength. Finally, the interaction between filaments is realized either by bonding or friction between filament surfaces.

Second, the cross-sectional area varies from filament to filament within the ensemble: $A_i(\chi) \neq A_j(\chi)$, where i, j are filament labels. Further, the disorder distribution in the bundle leads to two effects essentially influencing the overall behavior depending on the "wave pattern geometry": (1) in case of loose independent waves it results in delayed filament activation (also referred to as slack) and unequal stress distribution in filaments at a given control load, even under GLS, and (2) in case of wave geometry inducing pressure between filaments, e.g. spiral form in twisted yarns, it leads to higher interaction between filaments through friction and to damage localization in clusters.

Third, the most crucial part in the construction of the tensile experiment is the clamping of the yarn ends. In general, an ideal clamping is impossible and some kind of response distortion is always present. Therefore, it is important to construct the clamping in a way that allows us to factor out its influence from the measured response. In the applied experimental setup developed at the Institute for Textile Technology of the Aachen University, the yarn ends were fixed in epoxy resin (Gries and Royé, 2003). Without going into details of this setup we summarize the sources of distortion of the measured response that must be considered: First, the length of the individual filaments l_i varies due to the uneven surface of the epoxy resin (see Fig. 3a). This effect was observed both for yarns with a flat cross-sections as well as with a circular cross-section arrangement. Second, for short specimens the deformation of the epoxy resin cannot be neglected
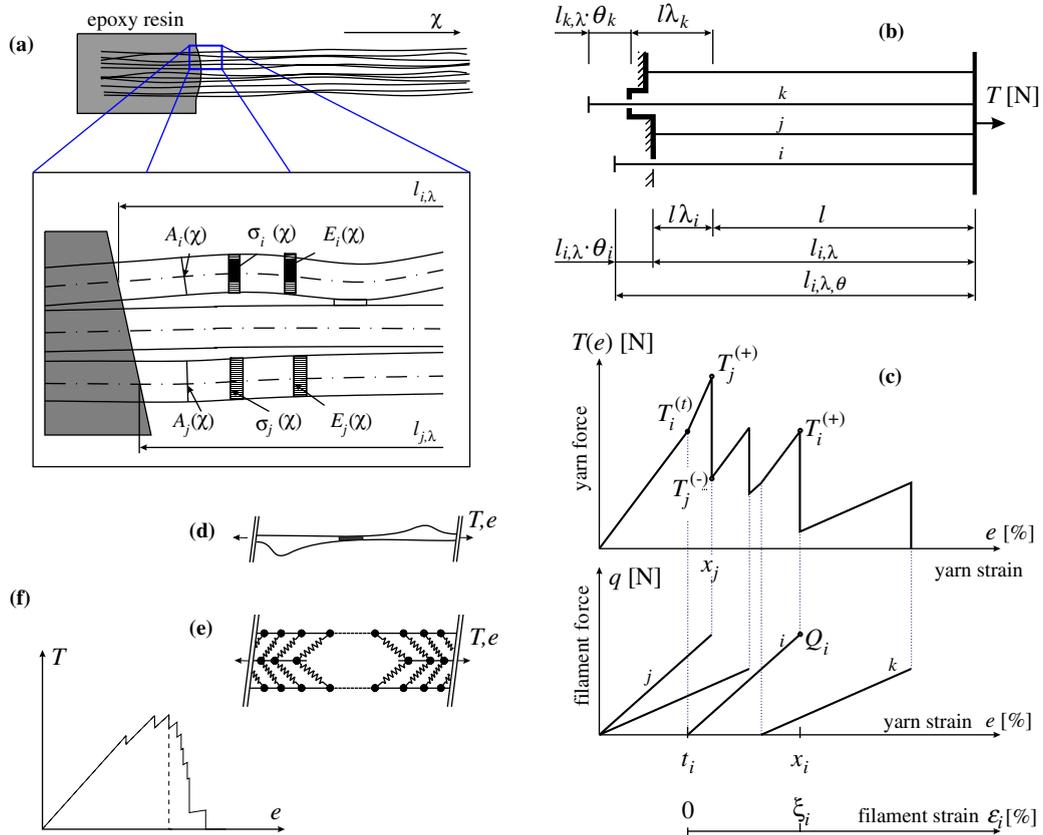
Fig. 3. (a) Elementary characteristics of filaments and their ordering in the yarn. (b) Physical model. (c) Mathematical model: superposition of the filament response with varying filament strength, stiffness, length and activation strain. (d) Stiffness activation through shear for delayed activation. (e) Overloading of two elements in the neighborhood of failed element under LLS rule. (f) Comparison of bundle load–strain diagrams without and with significant shear interaction between filaments.

since it significantly distorts the measured deformation. Third, in the post-peak region, the epoxy resin gets unloaded and contracts with an uncontrolled rate so that the loading rate of the bundle itself gets significantly increased especially for short specimens. Since the forces transmitted by short and long yarns are comparable and the deformable epoxy-made clamping is kept identical, the resulting diagram is distorted mainly for short specimens. Corrected diagrams (deformation of epoxy resin subtracted) are presented in Fig. 2(right). Later in the paper, we shall review this rather drastic correction and discuss more detailed interpretation of the changes in bundle-stiffness.

3. Computational model

The full coverage of the specified elementary effects would be possible using the finite element model including the specified sources of randomness. However, by realizing that we are dealing with bundles consisting of up to 3000 filaments with relatively dense discretization (e.g. for short autocorrelation structure of the spatially fluctuating material properties) we have to conclude that the computational complexity of the deterministic model makes the statistical evaluation by means of the Monte-Carlo computation impracti-

cable due to the prohibitive computational cost. In particular, with n number of filaments and p number of elements (material points) along each filament the order of structural stiffness matrix becomes $n(p + 1)$. In case that shear interaction is modeled in adjacent nodes, the stiffness/structural matrix is a symmetric band diagonal matrix with the number of nonzero elements equal to circa $n(p + 1)(n + 1)$. In a realistic case of $n = 1600$ and $p = 99$ the number of nonzero elements is $1600 \times 100 \times 1601 = 256.16 \times 10^6$. For double precision numbers, this corresponds to memory size of 2 GB and is obviously unaffordable for stochastic nonlinear computation even using today's high performance computers.

In case that no interaction between filaments is taken into account the structural matrix is tridiagonal so that, using the symmetry, the number of nonzero entries is $2n(p + 1)$. This corresponds to a moderate size of the system matrix of 2.6 MB. However, using the finite element discretization with Newton–Raphson scheme to trace the load–displacement diagram for this problem would still be like using a sledge hammer to crack a nut. As far as the friction between filaments remains negligible, as observed for the studied AR-glass yarns, it is possible to evaluate the bundle response during the displacement-controlled loading process explicitly, both analytically and numerically.

3.1. Kinematic model and constitutive law

We distinguish two kinds of parameters (see Fig. 3a): those appointed to ith filament and those appointed to whole filament ensemble:

(1) The parameters of ith filament make sense independently on the bundle composition. In case of AR-glass, linear elastic brittle behavior can be assumed with the parameters E_i for Young's modulus, σ_i for strength and A_i for cross-sectional area. We note that these parameters are assumed constant along the filament here and that the effect of their variability along χ will be taken into consideration in the companion paper.

(2) The bundle parameters quantify the differences between the filaments in the ensemble. Except of the probability distribution functions of the filament properties $G_A(A_i)$, $G_E(E_i)$, $G_f(\sigma_i)$ we introduce two kinds of lengths of ith filament that are different from the nominal length l of the bundle (see Fig. 3b): (a) distance $l_{i,\lambda}$ between fixing points of ith filament in the initial state of loading and (b) total filament length $l_{i,\lambda,\theta}$ in unstretched state. This total length includes the potential slack length. With reference to Fig. 3b we note that $l_{i,\lambda} = (1 + \lambda_i)l$ and the total filament length thus becomes:

$$l_{i,\lambda,\theta} = (1 + \theta_i)l_{i,\lambda} = (1 + \theta_i)(1 + \lambda_i)l. \tag{1}$$

Here, $\lambda_i = (l_{i,\lambda} - l)/l$ is the ratio of the extra distance between the clamps to the nominal length (in the initial state of loading). The parameter $\theta_i = (l_{i,\lambda,\theta} - l)/l_{i,\lambda}$ is the local activation strain at which the filaments i starts to transmit force.

Now, we shall include all the mentioned parameters in the load–strain functional relation $q_\varepsilon(\varepsilon)$. The linear-elastic, brittle response of ith filament as a function of the filament strain ε_i is given as

$$q_{\varepsilon,i}(\varepsilon_i) = \begin{cases} 0 & \text{for } \varepsilon_i < 0, \\ E_i A_i \varepsilon_i & \text{for } 0 \leqslant \varepsilon_i \leqslant \xi_i, \\ 0 & \text{for } \xi_i < \varepsilon_i \end{cases} \tag{2}$$

with $\xi_i = \sigma_i/E_i$ standing for the breaking strain. For convenience, we rewrite this relation in a more compact fashion using the Heaviside (unit step) function ($H(z) = 0$ for $z < 0$ and $H(z) = 1$ elsewhere): $q_{\varepsilon,i}(\varepsilon_i) = E_i A_i \varepsilon_i H(\varepsilon_i)H(\xi_i - \varepsilon_i)$.

In order to include the variations of the parameters across the bundle, we have to relate Eq. (2) to the control bundle strain e using the compatibility of strains for the control displacement $u(\varepsilon_i) \equiv u(e) = el$. With

this condition and with the filament length expressed according to Eq. (1) the local strain in the ith filament becomes (see Fig. 3b)

$$\varepsilon_i = \frac{u - \theta_i l_{i,\lambda}}{l_{i,\lambda,\theta}} = \frac{el - \theta_i(1+\lambda_i)l}{l_{i,\lambda,\theta}} = \frac{e - \theta_i(1+\lambda_i)}{(1+\theta_i)(1+\lambda_i)}. \tag{3}$$

We note that in this form, the local strains are related to the actual filament length rather than to the nominal length ($\varepsilon_i = e - \theta_i$) as it was the case in the original work of Phoenix and Taylor (1973). Our modification renders correct results even for very short bundles ($l \approx l_{\mathrm{bridge}}$) with relatively large scatter of filament length and activation strain. Another example of a modified mapping between the local strains and the bundle strain has been presented by Phoenix (1979) with the purpose of reflecting the kinematics in the twisted yarn structures.

By substituting Eq. (3) into Eq. (2) we obtain the load level in ith filament for a given control strain e

$$q_{e,i}(e) = E_i A_i \frac{e - \theta_i(1+\lambda_i)}{(1+\theta_i)(1+\lambda_i)} H[e - \theta_i(1+\lambda_i)] H\left[\xi_i - \frac{e - \theta_i(1+\lambda_i)}{(1+\theta_i)(1+\lambda_i)}\right]. \tag{4}$$

The arguments of the Heaviside jump functions can be used to obtain both the global activation strain t_i and the global breaking strain x_i of the ith filament as

$$t_i - \theta_i(1+\lambda_i) = 0 \rightarrow t_i = \theta_i(1+\lambda_i),$$
$$\xi_i - \frac{x_i - \theta_i(1+\lambda_i)}{(1+\theta_i)(1+\lambda_i)} = 0 \rightarrow x_i = \theta_i(1+\lambda_i) + \xi_i(1+\theta_i)(1+\lambda_i). \tag{5}$$

3.2. Numerical evaluation of the load–strain diagram for finite n

With reference to Fig. 3b we may use Eqs. (4) and (5) to obtain the overall load–strain diagram of the bundle as the sum of force contributions of all filaments at the fixed level of global strain

$$T(e) = \sum_{i=1}^{n} q_{e,i}(e) \tag{6}$$

with a minimum effort by using the following procedure:

(1) Assemble three vectors of n pairs $[e_j, T_j]$ of yarn strain and corresponding yarn force, namely $\boldsymbol{t}$ for activation strains and $\boldsymbol{x}^{(+)}$, $\boldsymbol{x}^{(-)}$ for breaking strains (Eq. (5)):

$$\left.\begin{aligned}
\boldsymbol{t} &= \left[t_j, T_j^{(t)}\right], &\text{where } T_j^{(t)} &= \sum_{i=1}^{n} q_{e,i}(t_j) \\
\boldsymbol{x}^{(+)} &= \left[x_j, T_j^{(+)}\right], &\text{where } T_j^{(+)} &= \sum_{i=1}^{n} q_{e,i}(x_j) \\
\boldsymbol{x}^{(-)} &= \left[x_j, T_j^{(-)}\right], &\text{where } T_j^{(-)} &= T_j^{(+)} - q_{e,i}(x_j)
\end{aligned}\right\} \quad j = 1,\ldots,n. \tag{7}$$

The force $T_j^{(-)}$ transmitted after the rupture of the jth filament is obtained by subtracting its contribution from $T_j^{(+)}$.

(2) The resulting load–strain diagram is constructed as a sorted union of the three vectors $\boldsymbol{t}$, $\boldsymbol{x}^{(+)}$ and $\boldsymbol{x}^{(-)}$: $\mathscr{R} = \cup\{\boldsymbol{t}, \boldsymbol{x}^{(+)}, \boldsymbol{x}^{(-)}\}$. The ordering is ascending and is given by the first pair member (yarn strain). If two pairs share the same strain then first comes the pair with the higher second member (force T_j). Mathematically this may be expressed as

$$\mathscr{R} := [e_j, T_j], \quad j = 1,\ldots,3n, \quad \text{where } \forall r_k, r_l \in \mathscr{R}, \quad k < l \Longleftrightarrow (e_k < e_l) \vee (e_k = e_l \wedge T_k > T_l). \tag{8}$$

The vector $\mathscr{R}$ represents a set of points of the piecewise-linear bundle load–strain diagram $T(e)$ that is plotted by connecting the points with straight lines (Fig. 3c).

The described algorithm uses the concept of superposition of the filament response (SFR) and provides an extremely efficient tool for numerical tracing of the bundle response with discrete resolution of filaments. Similar algorithm has been used to visualize damage patterns in the anti-plane analysis of a two-phase composite (Alzebdeh et al., 1998).

As already stated, this computation neglects any local interaction between filaments and corresponds to the GLS. Therefore, the model is only applicable if the influence of shear is small. Fig. 3e shows the localization of failure for a bundle after the rupture of a filament, a phenomenon that cannot be captured by the present model. Localization of failure into narrow zones due to shearing asserts mainly for long yarns providing sufficient length to build up forces comparable with the filament strength. Obviously, the increasing shearing capacity leads to more homogeneous force distribution within the bundle, and consequently to a more brittle failure as shown in Fig. 3f by the dashed line. In case of delayed activation, the increased shear transmission leads to faster activation of yarn stiffness due to the interaction of filaments between the waves (see Fig. 3d). Still, for the studied AR-glass yarns, the friction between filaments could been neglected. This simplification has been justified by the post-peak amount of friction observed in the tensile experiment and allowed us to use the GLS rule for stress redistribution upon a filament failure.

The evaluation of the tensile response in terms of the load–strain diagram $\mathscr{R}$ in Eq. (8) is absolutely inexpensive and, therefore, very suitable for the statistical analysis of random parameters varying both within the bundle cross-section and along the individual filaments. In order to introduce variations in parameters of the filament load–strain function given in Eq. (4) we shall summarize them in a vector parameter $\boldsymbol{\theta}_i$, so that

$$q_{e,i}(e) = q_{e,i,\theta}(e; \boldsymbol{\theta}_i) \quad \text{with } \boldsymbol{\theta}_i = \{A_i, E_i, \sigma_i, \theta_i, \lambda_i\}. \tag{9}$$

In the following studies the qualitative effect of variation in each of these parameters shall be visualized separately for selected distributions. Following the distribution, each filament gets associated with a separate instance of $\boldsymbol{\theta}_i$. Then, the load–strain diagram $\mathscr{R}$ is evaluated as described in Eqs. (4)–(8).

3.3. Continuous asymptotic model for infinite n

As n grows large, the mean load–strain diagram and the covariance function of load for two es can be obtained analytically as shown by Phoenix and Taylor (1973). In particular, the mean bundle response is obtained as n multiple of the mean filament response: $M_\theta(e) = n\mu_\theta(e)$. The effect of scatter of the vector parameter $\boldsymbol{\theta}$ on the mean filament response is evaluated using the integral form:

$$\mu_{\boldsymbol{\theta}}(e) = \int_{\boldsymbol{\theta}} q_e(e; \boldsymbol{\theta}) \, \mathrm{d}G_{\boldsymbol{\theta}}(\boldsymbol{\theta}) \tag{10}$$

with $G_i(\theta_i)$ standing for the cumulative probability distributions of the parameter θ_i. Filament behavior is governed by the global constitutive law (Eq. (4), index i dropped). For example, the mean load–strain curve for variable delayed activation θ is explicitly given as

$$\mu_{\theta}(e) = \int_{\theta} q_e(e; \theta) \, \mathrm{d}G_{\theta}(\theta). \tag{11}$$

There are two ways to interpret this equation: From a statistical point of view the mean filament load–strain diagram $\mu_\theta(e; \theta)$ represents an average filament response for infinite number of realizations of a single filament test $q_e(e; \theta)$ with the scatter of θ governed by the distribution $G_\theta(\theta)$. Alternatively, the integral

evaluation of the mean bundle load $M_\theta(e) = n\mu_\theta(e)$ can be seen in analogy with the discrete numerical evaluation of the bundle force $T(e)$ in Eq. (6) by summing filament contributions over the cross-section at a given bundle strain e. Similarly, in Eq. (11) we perform integration over fractions of distribution $G(\theta)$ at a given bundle strain e. In this view, the yarn corresponds to a homogeneous frictionless one-dimensional bar with the cross-sectional area nA.

The integral formulation shall be used in the sequel to verify the results of the numerical model. For special distribution functions the integral renders explicit analytical load–strain relation that may be even converted to an analytical formula of the mean size effect, i.e. an explicit expression for the mean strength as a function of the yarn length. However, the applicability of the analytical expressions for asymptotic mean and covariance is limited to the verification of numerically obtained results. One reason is that both the statistical moments and shape of the distribution is unknown for finite n even though the asymptotic form of peak load distribution for $n \to \infty$ is known (Daniels, 1945, 1989; Phoenix and Taylor, 1973). Another good reason for using the discrete numerical model is the possibility to study the effect of spatial randomization of filament properties (in the companion paper).

Using the introduced models we may now approach to parametric studies of the scatter of material parameters on the overall response accompanied with evaluation and discussion of the resulting length-dependent performance.

4. Parametric studies

In the examples below we study the influence of randomness of each single parameter separately and in combination if the parameters exhibit interactions. In this paper, the study is limited to the parameters λ, θ and A varying across the bundle: $i = 1, \ldots, n$. The effect of randomized parameters E, σ and n is studied in the companion paper (Vořechovský and Chudoba, 2006). The filament material is AR-glass with the following material parameters $\sigma = 1.25$ GPa, $E = 70$ GPa, diameter $D = 26$ μm and the corresponding breaking strain is given as $\xi = \sigma/E = 1.786\%$. In case of a perfect bundle the load–strain diagram can be simply written as $T(e) = M_0(e) = nEAeH(\xi - e)$.

For the sake of simplicity, in discrete bundle model we use 16 filaments only, while the real number of filaments in the studied yarn is approximately 100 times higher. In order to have the resulting forces in the figures comparable to the real values, the forces are given in cN. Diagrams of the mean bundle response obtained analytically using Eq. (10) are always plotted with dashed line for comparison.

4.1. Scatter of filament lengths

As mentioned previously, in the applied experimental setup the yarn ends were fixed in epoxy resin enfolding all the filaments in the cross-section. The cut through the clamping in Fig. 6(left) shows that the yarn cross-section has been homogeneously penetrated by the resin and enables gradual transmission of force into the individual filaments. The difficulty with this kind of clamping is that the resin penetrates also in the χ-direction (see Fig. 3a) with the consequence that the individual filaments have different lengths. For the purpose of the parametric study we introduce $l_{min} = \min_{i=1,\ldots,n}(l_{i,\lambda})$, $l_{max} = \max_{i=1,\ldots,n}(l_{i,\lambda})$ and $\Delta_{max} = l_{max} - l$, $\Delta_{min} = l_{min} - l$. In the load–strain diagrams shown in Fig. 4 we set the nominal length equal to the shortest filament length ($l = l_{min}$, $\Delta_{min} = 0$) and $\Delta_{max} = 2$ mm roughly corresponding to 1 mm maximum unevenness at both ends of the yarn. The diagrams in Fig. 4 are plotted for the nominal lengths 100, 50, 10, 5, 1 and 0.5 mm with constant E, σ, A and zero slack $\theta = 0$. Further, the distribution of relative length differences in the range $\lambda_i \in \langle 0, \lambda_{max} = \Delta_{max}/l \rangle$ is assumed uniform: $g_\lambda(\lambda) = 1/\lambda_{max}$ for $0 \leqslant \lambda \leqslant \lambda_{max}$ and $g_\lambda(\lambda) = 0$ elsewhere.
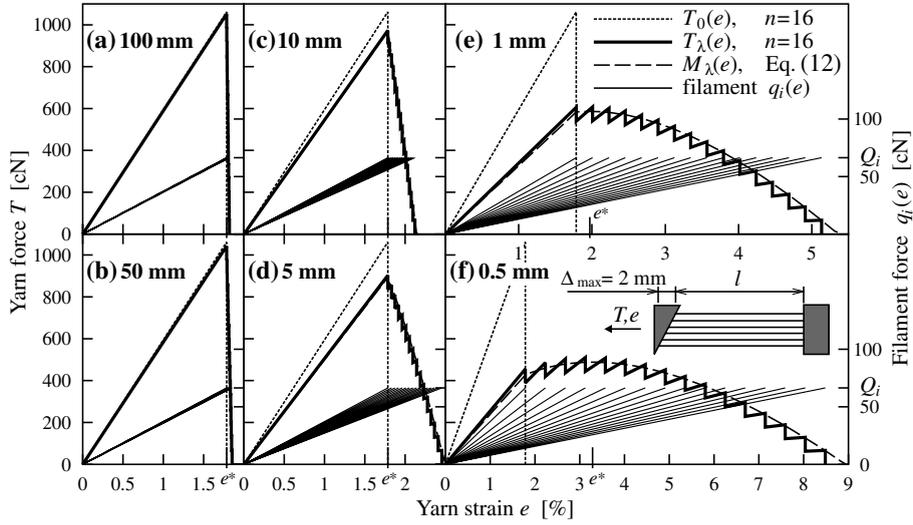
Fig. 4. The influence of distributed addition of 0–2 mm to the nominal length l = (a),...,(f), λ_{max} = 2/100, 2/50, 2/10, 2/5, 2/1, 2/0.5, respectively.

We remark that the choice of the nominal length l is arbitrary in the evaluation of $T(e)$ or $M(e)$. The use of the shortest filament is a natural choice in the present study. Obviously, a different choice of l leads to a different scaling of the response diagram along the horizontal axis e.

As can be seen in Fig. 4 the scatter of filament length leads to scatter of filament stiffness. As a result, the maximum strength cannot be reached simultaneously in all filaments which causes reduction of the maximum tensile force transmitted by the yarn. This is especially true for short specimens (Fig. 4c and d) with relatively ductile failure. The examples in Fig. 4e and f represent the qualitative tendencies in filament length variations approaching the condition of a crack bridge. In these cases the nominal length is shorter than the maximum additional length of 2 mm.

For infinite number of filaments, zero slack $\theta = 0$ and uniform distribution of $\lambda \sim R$: $g_\lambda(\lambda) = 1/\lambda_{max}H(\lambda)H(\lambda_{max} - \lambda)$ Eq. (10) reads

$$\mu_\lambda(e; \lambda \sim R) = \int_\lambda q_e(e;\lambda)\,dG_\lambda(\lambda) = \frac{EAe}{\lambda_{max}} \int_0^{\lambda_{max}} \frac{1}{(1+\lambda)}H[\xi(1+\lambda) - e]\,d\lambda$$

$$= \begin{cases} EAe \ln(1+\lambda_{max})/\lambda_{max} & 0 \leqslant e \leqslant \xi \quad \text{(linear)}, \\ EAe \dfrac{\ln(1+\lambda_{max}) - \ln(e/\xi)}{\lambda_{max}} & e > \xi \quad \text{(nonlinear)} \end{cases} \tag{12}$$

with its maximum $\mu_\lambda(e^*)$ lying either on the linear or nonlinear branch depending on the value of λ_{max}, see Table 1. For later discussion we remark that the mean prepeak stiffness reduces by the factor

$$r_\lambda = \ln(1+\lambda_{max})/\lambda_{max}. \tag{13}$$

Table 1
Mean peak load depending on λ_{max}

Case	(i) Fig. 4a–d	(ii) Fig. 4e and f
Condition	$\lambda_{max} \leqslant [\exp(1) - 1] \approx 1.718$	$\lambda_{max} > [\exp(1) - 1] \approx 1.718$
Strain at mean peak load e^*	ξ	$\xi(1+\lambda_{max})/\exp(1)$
Mean peak load $\mu_\lambda(e^*)$	$EA\xi\ln(1+\lambda_{max})/\lambda_{max}$	$EA\xi(1/\lambda_{max} + 1)/\exp(1)$
Asymptotic mean strength	$\lim_{\lambda_{max}\to 0}\mu_\lambda(e^*) = \mu_0(e^*) = EA\xi$	$\lim_{\lambda_{max}\to\infty}\mu_\lambda(e^*) = EA\xi/\exp(1)$
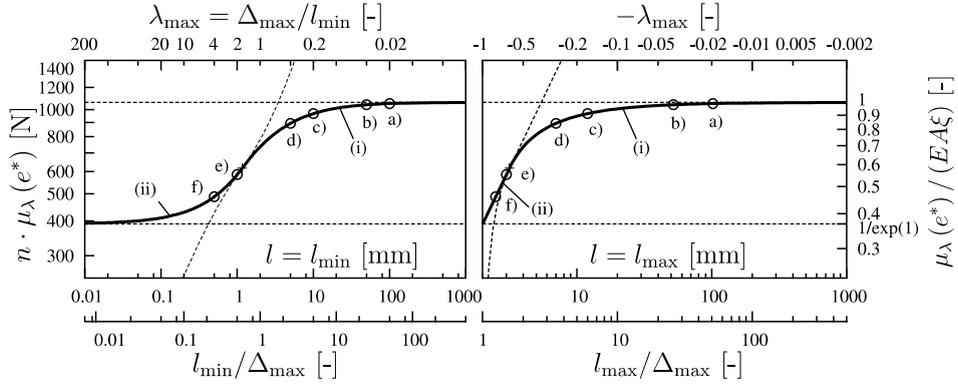
Fig. 5. Left: size effect for two different choices of nominal length (bi-logarithmic plot). Left: $l = l_{\min}$ ($\Delta_{\max} = 2$ mm). Right: $l = l_{\max}$ ($\Delta_{\min} = -2$ mm).

An explicit size effect equation in terms of nominal length $l = l_{\min}$ and constant $\Delta_{\max} = 2$ mm can now be obtained by the substitution $\lambda_{\max} = \Delta_{\max}/l$, in the previous paragraph:

$$\mu_\lambda(e^*; l = l_{\min}, \Delta_{\max}) = \begin{cases} EA\xi l \ln(1 + \Delta_{\max}/l)/\Delta_{\max} & \text{case (i),} \\ EA\xi(1 + l/\Delta_{\max})/\exp(1) & \text{case (ii).} \end{cases} \tag{14}$$

We note, that different form of the size effect equation is obtained with alternative definitions of the nominal length, e.g. with $l = l_{\max}$ and $\Delta_{\min} = -2$ mm so that $\Delta_{\max} = 0$ and $l + \Delta_{\min} \geqslant 0$ with negative $\lambda_{\max} = \Delta_{\min}/l$ (compare Fig. 5(left and right)):

$$\mu_\lambda(e^*; l = l_{\max}, \Delta_{\min}) = \begin{cases} EA\xi \dfrac{l + \Delta_{\min}}{\Delta_{\min}} \ln\left(1 - \dfrac{\Delta_{\min}}{l + \Delta_{\min}}\right) & \text{case (i),} \\ EA\xi \dfrac{l}{\Delta_{\min} \exp(1)} & \text{case (ii).} \end{cases} \tag{15}$$

In this formulation, the size effect is a linear function of l for short yarns (case ii) and nonlinear for long yarns (case i). This example illustrates that the variable λ is oriented and is negative for filaments shorter than l. By choosing different l we may change the scaling of the global strain e. As a consequence, the stiffness reduction introduced in Eq. (13) is valid only for case $l = l_{\min}$. By plotting the same diagrams for nominal length chosen as $l = l_{\max}$ and $\Delta_{\min} = -2$ mm, the short bundles would appear stiffer than the long ones. On the other hand, the choice of l has obviously no influence on the maximum bundle load.

The question of the right choice of the nominal length comes as a corollary of introducing the global bundle strain e. The proper choice of l becomes important when quantifying the bundle performance in a crack bridge. In such case an energetic considerations must be included in order to determine the correct effective bundle length.

We may conclude that the variations in the filament lengths act in an opposite way compared to statistical size effect. Second, this effect introduces ductile failure of short specimens (see Fig. 4). This contrasts with the response measured in the test (see Fig. 2(right)). The reason is the uncontrolled rate of unloading in the epoxy resin clamps resulting in increased loading rate of the bundle that is not reflected in the measuring equipment.

4.2. Scatter of filament diameters

The cross-sectional area of the filaments in the bundle exhibits relatively high scatter. In the particular case depicted in Fig. 6(left) the diameter takes values between 23 and 29 μm. Let us assume the variation of
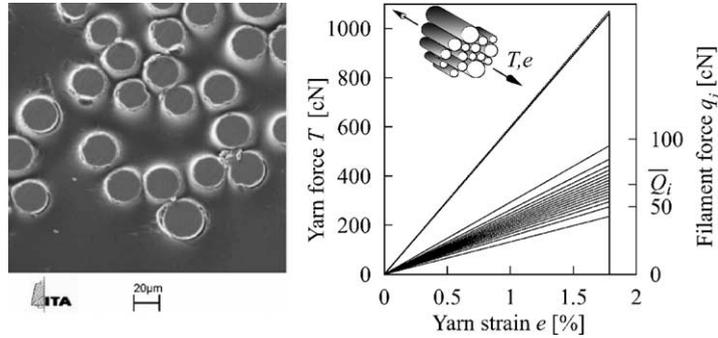
Fig. 6. Left: yarn penetrated by epoxy resin. Right: influence of scatter of filament diameters.

the filament diameter with the mean value $\bar{D} = 26$ μm and $COV(D) = 10\%$ (standard deviation 2.6 μm). With a cumulative distribution $G_D(D)$ and with $\lambda = \theta = 0$ the mean load–strain diagram introduced in Eq. (10) gets the form:

$$\mu_A(e; D) = eEH(\xi - e)\frac{\pi}{4}\int_D D^2 \, \mathrm{d}G_D(D). \tag{16}$$

We immediately see that all filaments fail simultaneously at the bundle strain $e = \xi$. Assuming a given diameter distribution $G_D(D)$ the ratio between the mean response of a bundle with and without scatter of D (taking its mean value) is obtained as

$$r_D = \frac{\mu_D(e)}{\mu(e)} = \frac{1}{\bar{D}^2}\int_D D^2 \, \mathrm{d}G_D(D).$$

In case of Gaussian distribution $G_D(D)$ this ratio reads $r_D = (1 + COV(D)^2)$. For the assumed value of $COV(D) = 10\%$ the mean bundle force (and mean bundle stiffness) gets increased by negligible amount of 1% (see Fig. 6(right)).

We may conclude that the scatter of the filament diameter does not significantly change the mean yarn response $M_A(e)$ compared to $M_0(e)$. However, it brings about a scatter of the load–strain response and the peak load.

4.3. Scatter of filament activation strain (slack)

The waviness of filaments leads to their delayed activation during the loading process. In order to study its qualitative influence on the response we have defined a uniform filament activation density function $g_\theta(\theta)$ (see Fig. 7) distributed over the activation range $0 \leqslant \theta \leqslant \theta_{\max}$. Considering $\lambda = 0$, $\theta_{\max}$ represents the activation strain of the last filament. For simplicity we again set the nominal length l equal to the length of the shortest filament.

The analytical solution of the integral equation (11) renders the mean filament load–strain diagram $\mu_\theta(e)$ consisting of three branches:

$$\mu_{\theta,1}(e) = \frac{EA}{\theta_{\max}}\int_0^e \frac{e-\theta}{1+\theta}\,\mathrm{d}\theta = \frac{EA}{\theta_{\max}}[(e+1)\ln(1+e) - e],$$

$$\mu_{\theta,2i}(e) = \frac{EA}{\theta_{\max}}\int_{\frac{e-\xi}{1+\xi}}^e \frac{e-\theta}{1+\theta}\,\mathrm{d}\theta = \frac{EA}{\theta_{\max}}(e+1)\left[\ln(1+\xi) - \frac{\xi}{1+\xi}\right],$$
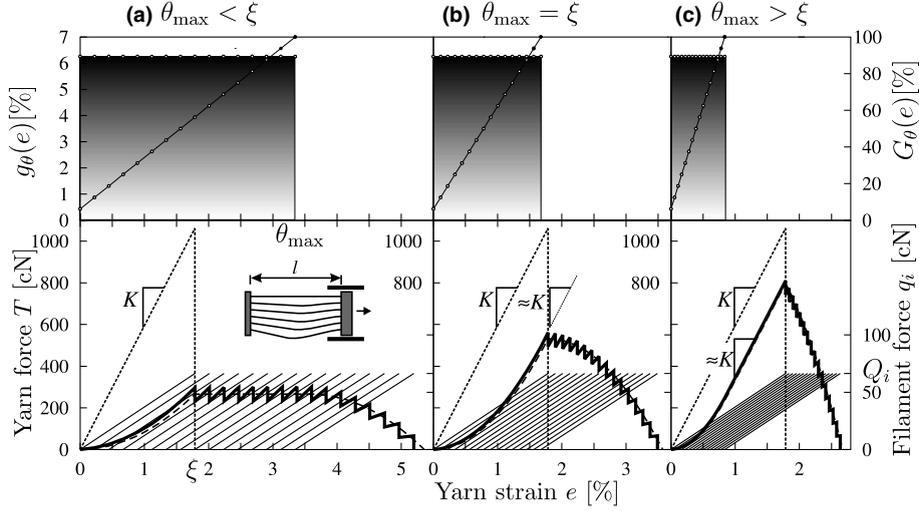
Fig. 7. Comparison of three constant densities of delayed activation.

$$\mu_{\theta,2ii}(e) = \frac{EA}{\theta_{\max}} \int_0^{\theta_{\max}} \frac{e-\theta}{1+\theta} \mathrm{d}\theta = \frac{EA}{\theta_{\max}} [(e+1) \ln(1+\theta_{\max}) - \theta_{\max}],$$

$$\mu_{\theta,3}(e) = \frac{EA}{\theta_{\max}} \int_{\frac{e-\xi}{1+\xi}}^{\theta_{\max}} \frac{e-\theta}{1+\theta} \mathrm{d}\theta = \frac{EA}{\theta_{\max}} \left\{ (e+1) \left[\ln\left(\frac{(1+\theta_{\max})(1+\xi)}{1+e} \right) \right] - \theta_{\max} + \frac{e-\xi}{1+\xi} \right\}. \tag{17}$$

(1) ascending with gradual increase of stiffness $e \in \langle 0, \min(\xi, \theta_{\max}) \rangle$ (filaments get only activated),
(2) ascending branch $e \in \langle \min(\xi, \theta_{\max}), \max(\xi, \theta_{\max}) \rangle$, is a linear function of strain e given by
    (i) $\mu_{\theta,2ii}$ if $\theta_{\max} < \xi$ (no activation and no breaks),
    (ii) $\mu_{\theta,2i}$ if $\theta_{\max} > \xi$ (both activation and breaks),
(3) generally ascending and descending branch $e \in \langle \max(\xi, \theta_{\max}), \theta_{\max} + \xi(1 + \theta_{\max}) \rangle$ (only breaks).

In Fig. 7 we illustrate the three qualitatively different forms of the load–strain diagram depending on the relation between $\theta_{\max}$ and ξ.

It is worth to note that the original formulation of Phoenix and Taylor (1973) leads to a simpler form of load–strain diagram (compare Fig. 8). The explicit formula can be obtained by integrating $\hat{\mu}_\theta(e) = EA/\theta_{\max} \cdot \int_{\theta_1}^{\theta_2} (e-\theta) \mathrm{d}\theta, \theta_1 = (0 \vee e - \xi), \theta_2 = (\theta_{\max} \vee e)$. In analogy with Eq. (17) the load–strain curve consisting of $\hat{\mu}_{\theta,1}$, $\hat{\mu}_{\theta,2i}$, $\hat{\mu}_{\theta,2ii}$ and $\hat{\mu}_{\theta,3}$ can be constructed using the four combinations of the given integration limits. As shown in Fig. 8 the main difference of this solution is that in case of $\xi < \theta_{\max}$ the second branch is a constant function (Fig. 9).

For the purpose of deriving the size effect equation it is sufficient to seek the maximum value $\mu_\theta(e^*)$ in the branch (3). The asymptotic mean peak load $\mu_\theta(e^*) = \mu_{\theta,3}(e^*)$ is attained at $e^* = \max(e_3^*, \xi)$ where e_3^* is a stationary point:

$$\frac{\mathrm{d}\mu_{\theta,3}(e)}{\mathrm{d}e} = 0 \rightarrow e_3^* = (1+\xi)(1+\theta_{\max})/\exp\left(\frac{\xi}{1+\xi}\right) - 1.$$

By substituting the action point e^* into $\mu_{\theta,3}(e)$: $\mu_\theta^* = \mu_{\theta,3}(e^*)$ and by taking $\theta_{\max} = \Delta_{\max}/l$ with $\Delta_{\max}$ a given constant, we obtain the size effect equation $\mu_\theta^*(l; \Delta_{\max})$ in terms of nominal length. The formula is rather complicated, but the noticeable fact is that the strength asymptote for extremely short yarns is constant:
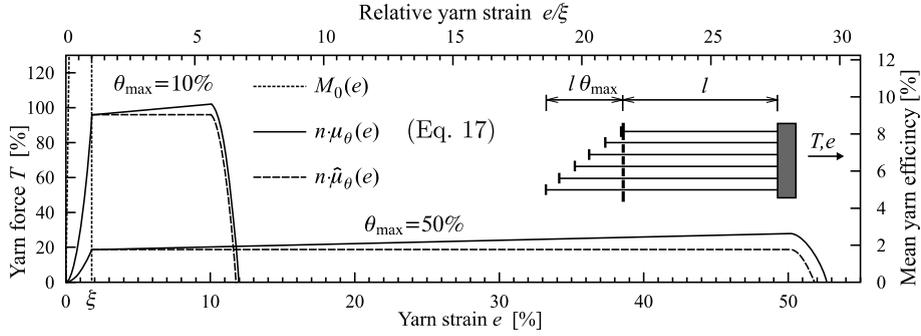
Fig. 8. Comparison of load–strain diagrams for uniform $G_\theta(\theta)$ with large θ_{max}/ξ according to Phoenix and Taylor (1973) (dashed line) and according to our kinematic assumption (solid line).
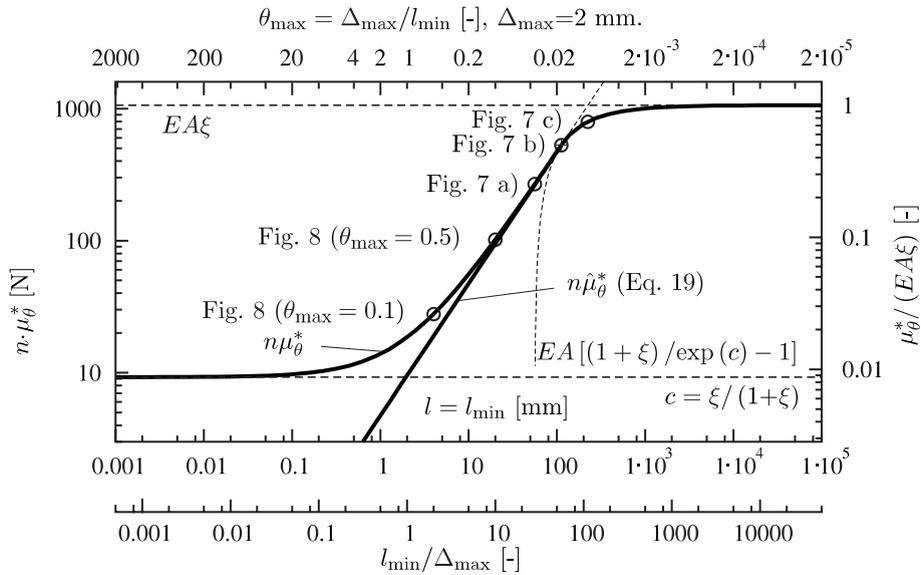
Fig. 9. Mean size effect curve for yarn with uniform delayed activation density. Comparison of the formulation due to Phoenix and Taylor (1973) and refined formulation based on Eq. (4).

$$\lim_{l \to 0} \mu_\theta^* = EA[(1 + \xi)/\exp(c) - 1], \quad c = \xi/(1 + \xi). \tag{18}$$

The size effect equation of $\hat{\mu}_\theta(e)$ again consists of two branches depending on the relation between θ_{max} and ξ:

$$\hat{\mu}_\theta^* = \hat{\mu}_\theta(l, \Delta_{max}) = \begin{cases} EA\xi^2/(2\theta_{max}) = lEA\xi^2/(2\Delta_{max}) & \xi \leqslant \theta_{max}, \\ EA(\xi - \theta_{max}/2) = EA\left(\xi - \frac{\Delta_{max}}{2l}\right) & \xi > \theta_{max}. \end{cases} \tag{19}$$

The asymptote of μ_θ^* for $l \to 0$ (Eq. (18)) is constant while $\hat{\mu}_\theta^*$ (Eq. (19)) linearly approaches zero. The different asymptotic response may be explained using Fig. 10. In the kinematic relation underlying the derivation of $\hat{\mu}_\theta^*$ the filament length is assumed equal to the nominal length l (Fig. 10(left)). As $l \to 0$ linearly the range of delayed activation given by $\theta_{max} \to \infty$ linearly as well. As a result, the load–strain diagram gets a form of a flat rectangle with dominating second branch $\hat{\mu}_{\theta,2ii}(e)$ and limit peak load approaching zero as
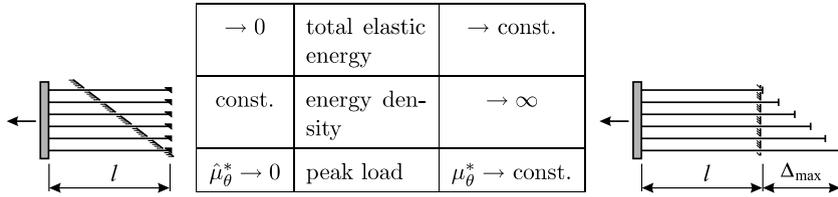
Fig. 10. Physical interpretation of slack in two models with resulting asymptotic behavior as $l \to 0$. Left: Phoenix and Taylor (1973). Right: definition according to Eq. (3).

shown in Fig. 8. On the other hand, in the refined case of μ_θ^*, the filament length is independent of the nominal length (Fig. 10(right)). The limit case $l \to 0$ corresponds to the bundle with the longest filament approaching $\Delta_{\max}$ with load–strain diagram getting a shape of triangle dominated by the second branch $\mu_{\theta,2it}(e)$ and a constant peak load. Both cases of asymptotic behavior are only theoretical and valid provided the number of filaments is infinite and the load is transmitted continuously. In the discrete case this is not true and the limiting bundle mean strength equals to the strength of a single filament. This is because there are no two filaments active simultaneously.

We conclude that delayed activation induced by waviness drowns the statistical size effect and must be included in the interpretation of the measured data in order to assess the length dependent strength of the bundle accurately. The effect of differences in filament lengths induced by θ on the evolution of bundle stiffness for $e \leqslant \xi$ is generally negligible as documented in Fig. 8.

4.4. Interaction of scatter of filament lengths and delayed activation

The mean load–strain curve with both effects included has the form of twofold integral

$$
\begin{aligned}
\mu_{\theta,\lambda}(e) &= \int_\theta \int_\lambda q_e(e; \theta, \lambda) \, \mathrm{d}G_\theta(\theta) \, \mathrm{d}G_\lambda(\lambda) \\
&= EA \int_\theta \int_\lambda \frac{e - \theta(1+\lambda)}{(1+\theta)(1+\lambda)} H\left[\xi - \frac{e - \theta(1+\lambda)}{(1+\theta)(1+\lambda)}\right] \cdot H[e - \theta(1+\lambda)] \, \mathrm{d}G_\theta(\theta) \, \mathrm{d}G_\lambda(\lambda).
\end{aligned} \tag{20}
$$

Even though θ and λ represent independent sources of imperfection (filament waviness and uneven clamps) their distributions $G_\lambda(\lambda)$ and $G_\theta(\theta)$ exhibit interactions induced by the chosen definition of strains (Eq. (3)). This means for example that the same $\theta_{\max}$ produces different effect on the response at different levels of $\lambda_{\max}$. The reason is that according to the kinematic hypothesis in Eq. (1) the relative extra length λ influences the extra length due to delayed activation in the form $\Delta_\theta = \theta l(1 + \lambda)$; in other words the slack length depends on the initial distance of fixing points.

The interaction is documented in Fig. 11(right) on the development of stiffness. For the sake of comparison with previous results we again assume uniform distributions $G_\lambda(\lambda)$ and $G_\theta(\theta)$. The reduction of mean prepeak stiffness due to scatter of λ has been expressed by factor r_λ (Eq. (13)). The stiffness obtained by applying r_λ to stiffness of $\mu_\theta(e)$ illustrated by the dotted line overestimates the real stiffness obtained for $\mu_{\lambda,\theta}(e)$ using Eq. (20).

The analysis of the interaction effect is important especially in the context of very short tensile tests and of crack bridges as documented in Fig. 11.

The situation close to our laboratory tests with $l = 30$ mm is shown in Fig. 11(left): $\lambda_{\max} = 2/30 = 0.0\overline{66}$, $\theta_{\max} = 0.009$. We see that the effect of different lengths can be neglected even in the shortest tested bundle. This justifies the correction of stiffness of the bundle test made in Fig. 2(right).

Fig. 11(right) shows the possible situation in crack bridges: $\lambda_{\max} = 1.2$ meaning that the furthest points are 2.2 times further than the closest ones. The maximum slack $\theta_{\max} = 1.2\xi = 0.0214$. ($\lambda_{\max}$ here is 18 times
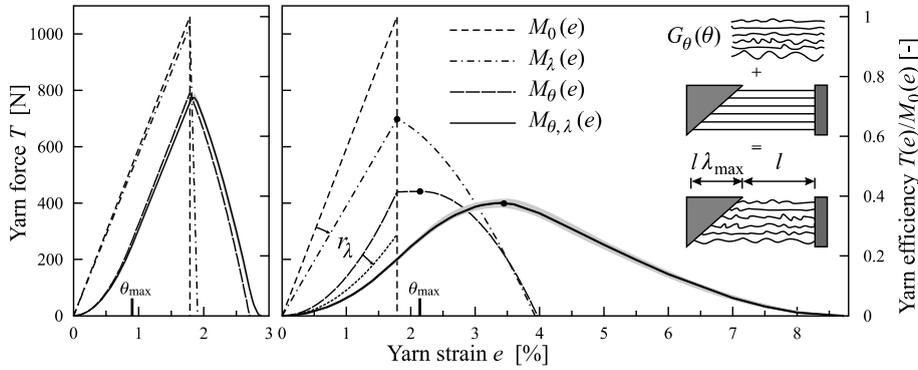
Fig. 11. Interaction of scatter of λ and θ. Left: situation of a yarn tensile test. Right: situation of a crack bridge.

higher than before, θ_{max} is 2.38 times larger than before). We note that the interaction shifts the action point e^* to the right, here it can be reasonably approximated as $e^* = (1 + \lambda_{max}/2) \cdot \max(\theta_{max}, \xi)$. This approximation may help to narrow the region of numerical evaluation of integral equation (20) in the construction of the mean size effect curve.

5. Correspondence between the delayed activation and waviness

In order to provide the correct interpretation of the experimental data we need to explain the qualitative correspondence between the waviness and the delayed activation. As shown in Fig. 12, the activation density function changes with the length of the specimen. During the production of the yarn and during the preparation of the experimental setup several wave patterns may be included in the yarn structure. It is helpful to classify the fundamental wave patterns according to their influence on the delayed activation with respect to the changing nominal specimen length l (Fig. 12). We may distinguish the following three limiting cases: (A) length differences growing linearly with l leading to length independent delayed activation and (B) averaging of length differences and diminishing delayed activation for increasing l. In order to answer the question which case is relevant for a particular type of yarn we evaluate the delayed activation for selected types of waviness shown in Fig. 13. The study includes patterns (a) and (b) that are introduced during the production process, (c) arising during the test preparation, and (d) appearing during the packaging.
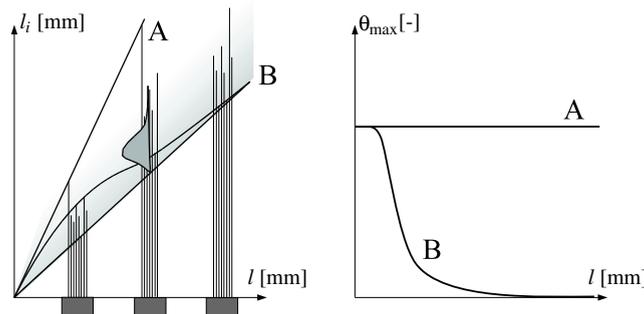
Fig. 12. Distribution of relative extra length for changing nominal length and possible shapes of maximum slack θ_{max}.

(a) $w = \sin\left(\dfrac{2\pi}{T}(\chi - \phi_i)\right)$, $\phi_i = \dfrac{\Phi i}{n-1}$ **(b)** $w = a_i \sin\left(\dfrac{2\pi}{T}\chi\right)$, $a_i = \dfrac{ai}{n-1}$

(c) $w = a_i \sin\left(\dfrac{2\pi}{l}\chi\right)$, $a_i = \dfrac{a\sqrt{i}}{n-1}$ **(d)** $l_i = \pi r_i$, $r_i = r + \dfrac{(R-r)i}{n-1}$
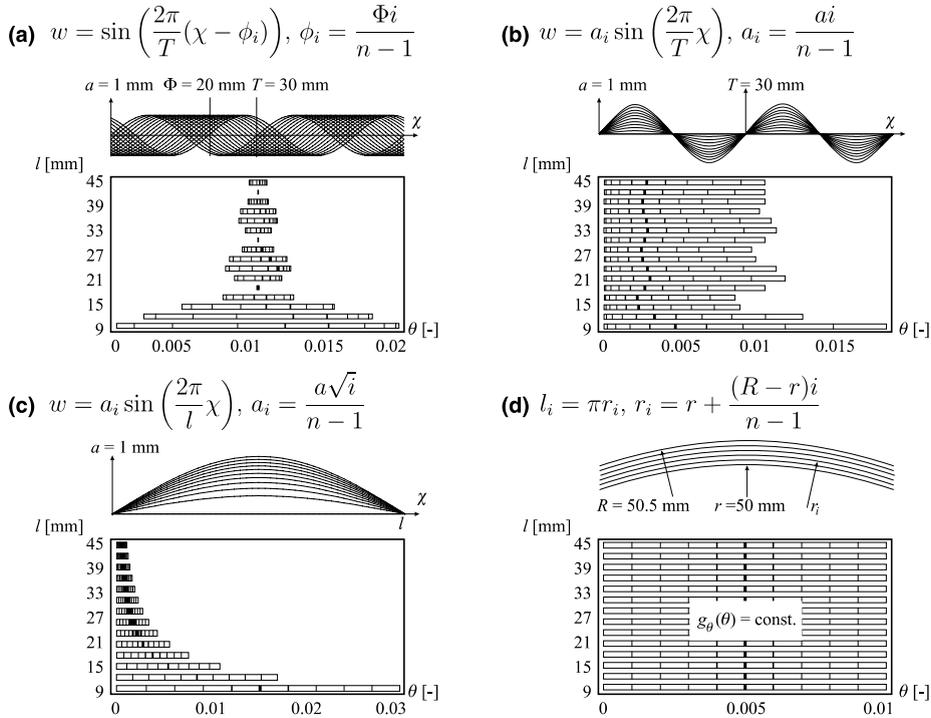
Fig. 13. Wave patterns with corresponding activation profiles ($i = 0, \ldots, (n-1)$).

Let the filament geometry within the bundle be defined by the wave function $w(\chi, \alpha)$, where $\alpha \in \langle 0, 1 \rangle$ is the parameter specifying the filament position within the bundle. The total length of a single filament is computed as $l_i = \int_0^l \sqrt{1 + w(\chi, \alpha)'^2}\, d\chi$ and the activation strain is obtained as $\theta_i = (l_i - l)/l$ (provided $\lambda_i = 0$). The estimation of the activation density corresponding to the wave pattern can then be constructed as a histogram of θ_i, $i = 1, \ldots, n$. In Fig. 13 we show the four selected types of $w(\chi, \alpha)$ with the obtained histograms θ_i for varied nominal length. The histograms are plotted as bars divided in 10 segments, each representing 10% fraction of filaments with corresponding activation strain range. We assume that filaments do not hinder each other in deformation so that no modification of the formulation of local strains is needed.

The first wave pattern (a) consists of periodic waves with equal amplitudes shifted by Φ_i in χ-direction. The corresponding ranges of activation strains oscillate around the limiting activation strain (approximately 1.1%). For large l the differences in filament lengths become negligible and the influence of delayed activation disappears (case B in Fig. 12).

The second pattern (b) consists of regular periodic waves with a uniform distribution of amplitudes a_i. The corresponding histograms show that most of the filaments get activated in the beginning of loading. After a few oscillations this kind of wave pattern leads to the stabilized length-independent delayed activation for sufficiently long specimens (case A in Fig. 12).

The third pattern (c) shows a single wave over the nominal length l. There is a higher fraction of filaments with larger amplitudes. The chosen linear distribution of amplitudes results in uniform activation density functions that get reduced to simultaneous activation for large l (case B).

The last pattern (d) shows the length distribution resulting from the coiling of the yarns onto the bobbins. Obviously, this length distribution leads to uniform delayed activation density that does not change with the length l. The length differences scale up linearly with the nominal length (case A in Fig. 12).

The performed geometrical classification of wave patterns will be used in the next paragraph to assess the plausibility of the identified delayed activation density and to make inferences about the dominating patterns in the structure of the studied yarn.

6. Identification of the parameter distributions

In the majority of cases the nonlinearity of the load–strain curve in the initial stages of loading can be assigned solely to the scatter of activation strains. Therefore, the initial part of the response curve lends itself for an isolated identification of the activation density. In particular, its determination may be held separately upon the following conditions:

- All filaments have been activated at the onset of breaking: $\theta_{\max} \leqslant \xi$ provided $0 \leqslant \theta \leqslant \theta_{\max}$. This condition is fulfilled for all studied specimen lengths.
- Interaction effects of λ and θ discussed in Section 4.4 can be neglected. This is true for all studied specimen lengths as documented in Fig. 11(left) on the shortest specimen.
- Other discrepancies do not disturb the curve $T(e)$ (such as differences in E-modulus etc.) rendering this estimation too rough.

As suggested by Phoenix (1974) the cumulative density of delayed activation $G_\theta(\theta)$ can be determined directly from the measured load–strain data $T_{\text{test}}(e)$ by constructing its normalized derivative:

$$G(\theta) \approx \frac{1}{k_{\max}} \frac{\mathrm{d}T_{\text{test}}(e)}{\mathrm{d}e}, \quad k_{\max} = \max_{\forall e} \frac{\mathrm{d}T_{\text{test}}(e)}{\mathrm{d}e}.$$

However, in our case it was rather tedious to construct the numerical derivative from the available $T_{\text{test}}(e)$ curves so that we decided to perform an indirect matching of the model $T(e)$ based on the predefined shape of the activation density function. The selected profile of the activation density function $g(\theta)$ is a piecewise linear function with four parameters (see diagrams in left Fig. 15).

The densities obtained by fitting are shown in the left four diagrams of Fig. 15 and re-plotted as a sequence of histograms in Fig. 14(left) in order to make them comparable with the densities resulting from the wave patterns studied in Section 5. Considering first the evolution of the activation range in terms of $\theta_{\max}$ we see that its change is negligible between $l = 220$ and $l = 500$ mm. This suggests the existence of patterns (b) and (d). Comparing the profile of the activation density function we observe that most of the filaments get activated in the beginning of loading so that the yarn structure more likely exhibits features of (b) than of (d). Furthermore, the existence of the periodic structure (b) is supported visually as can be seen in Fig. 14(right). For short specimens ($l = 45$ mm and $l = 30$ mm) the effect of periodicity becomes negligible since the specimen length is in the range of the wave period $l \approx T$. The activation range $\theta_{\max}$ gets larger and its profile approaches uniform activation density. Such tendency may be ascribed to the wave pattern (c) resulting from imperfections in clamping in the preparation of short specimens.
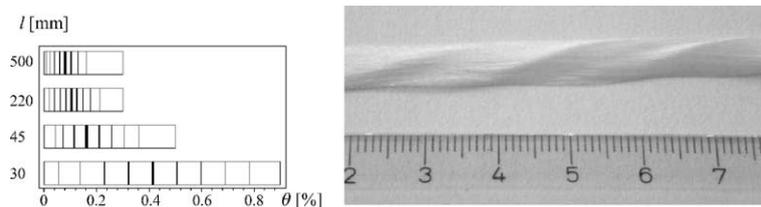
Fig. 14. Left: activation density function reflecting the tensile tests. Right: waves in the tested yarn.
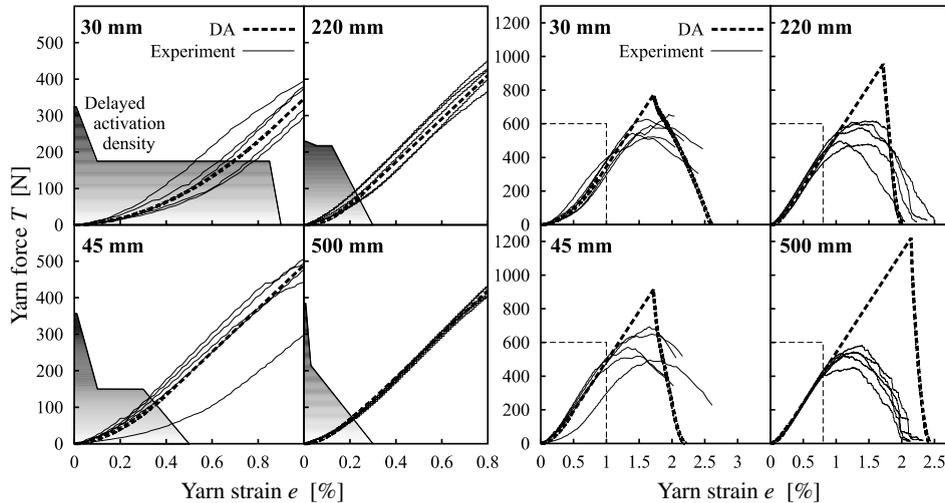
Fig. 15. Delayed activation densities and load–strain curves (experiment and simulation). Left: zoom into $T(e)$ diagrams displayed on the right.

The load–strain curves calculated for the considered lengths using the obtained activation densities are plotted in the right four diagrams of Fig. 15. In agreement with the studies in Section 4.3 we observe an increase of the peak load for longer test specimens due to the isolated effect of delayed activation. This tendency contrasts with the statistical size effect in the traditional sense bringing about strength reduction for longer specimens.

Obviously, the experimental data must be interpreted as a combination of several effects and the size effect must be considered in a complex sense: including sources of randomness affecting local strength and/or stiffness both across and along the bundle. The evaluation of such a complex size effect on the example of the studied yarn is deferred until the last section of Part II.

7. Conclusions

In order to study the effect of disorder in the yarn structure and of imperfections in the experimental setup we have applied a strain-based formulations of a fiber bundle model in two versions: (1) continuous analytical model according to Phoenix and Taylor (1973) and (2) discrete numerical model based on the superposition of filament load–strain diagrams (SFR). Both formulations have been equipped with a refined constitutive law based on a kinematic hypotheses with improved representation of local strains. As we could document on examples, this extension results in strong nonlinearity of mean size effect curve for short yarns with large disorder.

The simulations have been done with reference to the experimental data obtained from the tensile test on AR-glass yarns 2400 tex with varied specimen length. The applied models do not include local load sharing upon filament failure. Such a simplification was justified for the studied type of yarn since the global load sharing clearly dominated. The modeling concept allowed us to separate and quantify the distorting effects of the experimental setup from the response data and make the interpretation of the experimental results feasible.

The analyses were focused on irregularities across the bundle, namely scatter of filament length, scatter of filament diameter and scatter of activation strain. The analysis of scatter along the filaments has been

postponed until Part II. The parametric studies using both the analytical and the numerical model have shown that the scatter of filament lengths and filament waviness strongly reduce the efficiency of yarns with short effective lengths. Further, we could identify a strongly nonlinear dependence of the statistical slack distribution on the bundle length or eventually on the distribution of filament lengths (clamp distances) across the bundle. These sources of strength reduction must be included in the performance assessment of the quasi-ductile composites with dry yarns acting in crack bridges on extremely short lengths.

The discrete numerical model developed in this paper provides a tool for thorough analysis of interacting sources of disorder in the bundle. It serves as a basis for stochastic analysis of the complex size effect comprising all the introduced effects, including the influence of finite number of filaments in the bundle. The modeling technique employing the random field simulation and the evaluation of the complex size effect is described in detail in the companion paper (Vořechovský and Chudoba, 2006).

Acknowledgments

References

Alzebdeh, K., Al-Ostaz, A., Jasiuk, I., Ostoja-Starzewski, M., 1998. Fracture of random matrix-inclusion composites: scale effects and statistics. International Journal of Solids and Structures 35 (19), 2537–2566.

Beyerlein, I.J., Phoenix, S.L., 1996. Comparison of shear-lag theory and continuum fracture mechanics for modeling fiber and matrix stresses in an elastic cracked composite lamina. International Journal of Solids and Structures 33 (18), 2543–2574.

Beyerlein, I.J., Phoenix, S.L., 1997. Statistics of fracture for an elastic notched composite lamina containing Weibull fibers. Part I: features from Monte-Carlo simulation. Engineering Fracture Mechanics 57 (2/3), 241–265.

Coleman, B.D., 1958. On the strength of classical fibres and fibre bundles. Journal of the Mechanics and Physics of Solids 7, 60–70.

Curbach, M., 2002. Arbeits- und Ergebnisbericht zum Sonderforschugsbereich 532 Textile Bewehrung zur Bautechnischen Verstärkung und Instandsetzung' für die Periode II/1999 bis I/2002. Technical Report SFB528, Technical University Dresden, 2002 (in German).

Curbach, M., Hegger, J. (Eds.), 2001. Textilbeton—1. Fachkollquium der Sonderforschungsbereiche 528 und 532. RWTH Aachen, 2001 (in German).

Daniels, H., 1945. The maximum of a Gaussian process whose mean path has a maximum, with an application to the strength of bundles of fibres. Advances in Applied Probability 21, 315–333.

Daniels, H.E., 1989. The statistical theory of the strength of bundles of threads. Proceedings of the Royal Society (London) 183A, 405.

Fisher, R.A., Tippett, L.H.C., 1928. Limiting forms of the frequency distribution of the largest and smallest member of a sample. Proceedings, Cambridge Philosophical Society 24, 180–190.

Gries, T., Royé, A., 2003. Three-dimensional reinforcement structures for thin walled components. In: Curbach, M. (Ed.), 2nd Colloquium on Textile Reinforce Structures (CTRS2), Dresden, 2003, pp. 513–524.

Harlow, D.G., Phoenix, S.L., 1978a. The chain-of-bundles probability model for the strength of fibrous materials. II. A numerical study of convergence. Journal of Composite Materials 12, 314–335.

Harlow, D.G., Phoenix, S.L., 1978b. The chain-of-bundles probability model for the strength of fibrous materials. I. Analysis and conjectures. Journal Composite Materials 12, 195–214.

Hegger, J., 2002. Arbeits- und Ergebnisbericht zum Sonderforschugsbereich 532 'Textilbewehrter Beton: Grundlagen für die Entwicklung einer neuartigen Technologie' für die Periode II/1999 bis I/2002. Technical Report SFB532, Aachen University, 2002 (in German).

Hidalgo, R.C., Moreno, Y., Kun, F., Hermann, H.J., 2002. Fracture model with variable range of interaction. Physical review E 65, 046148.

Ibnabdeljalil, M., Curtin, W.A., 1997. Strength and reliability of fiber-reinforced composites: localized load sharing and associated size-effects. International Journal of Solids and Structures 34 (21), 2649–2668.

Krajcinovic, D., Silva, M.A.G., 1982. Statistical aspects of the continuous damage theory. International Journal of Solids and Structures 18 (7), 551–562.

Kun, F., Zapperi, S., Herrmann, H.J., 2000. Damage in fiber bundle models. The European Physical Journal B (17), 269–279.

Phoenix, S.L., 1974. Probabilistic strength analysis of fibre bundle structures. Fibre Sciences and Technology 7, 15–31.

Phoenix, S.L., 1975. Probabilistic inter-fiber dependence and the asymptotic strength distribution of classic fiber bundles. International Journal of Engineering Science 13, 287–304.

Phoenix, S.L., 1978. The random strength of series-parallel structures with load sharing among members. Probabilistic Mechanics, 91–95.

Phoenix, S.L., 1979. Statistical theory for the strength of twisted fiber bundles with applications to yarns and cables. Textile Research Journal, 407–423.

Phoenix, S.L., Taylor, H.M., 1973. The asymptotic strength distribution of a general fiber bundle. Advances in Applied Probability 5, 200–216.

Phoenix, S.L., Ibnabdeljalil, M., Hui, C.Y., 1997. Size effects in the distribution for strength of brittle matrix fibrous composites. International Journal of Solids and Structures 34 (5), 545–568.

Smith, R.L., Phoenix, S.L., 1981. Asymptotic distributions for the failure of fibrous materials under series-parallel structure and equal load-sharing. Journal of Applied Mechanics 48, 75–82.

Vořechovský, M., Chudoba, R., 2006. Stochastic modeling of multi-filament yarns: II. Random properties over the length and size effect. International Journal of Solids and Structures, doi:10.1016/j.ijsolstr.2005.06.062.

Weibull, W., 1939. The phenomenon of rupture in solids. Royal Swedish Institute of Engineering Research (Ingenioersvetenskaps Akad. Handl.), Stockholm 153, 1–55.

Zhou, S.J., Curtin, W.A., 1995. Failure of fiber composites: a lattice green function model. Acta Metallurgica Material 43 (8), 3093–3104.